双模板法制备具有介孔孔壁的三维有序大孔二氧化铈及其改善的低温还原性能

张　晗，张　磊，邓积光，刘雨溪，蒋海燕，石凤娟，吉科猛，戴洪兴[*]

北京工业大学环境与能源工程学院化学化工系，北京 100124

摘要：以聚甲基丙烯酸甲酯 (PMMA) 为硬模板，三嵌段共聚物 F127、十六烷基三甲基溴化铵 (CTAB) 或聚乙二醇 (PEG) 为软模板剂 (表面活性剂)，柠檬酸为络合剂，硝酸铈为金属前驱体，采用双模板法成功地合成出具有介孔孔壁的三维有序大孔 (3DOM) 结构的立方相 CeO_2 样品 CeO_2-F127, CeO_2-CTAB 和 CeO_2-PEG，并利用多种分析技术表征了它们的物化性质. 结果表明，三个样品均具有 3DOM 结构和蠕虫状介孔孔壁，表面活性剂的种类对样品的孔结构和比表面积影响较大. 在制备过程中引入表面活性剂可提高 CeO_2 样品的比表面积，所得 CeO_2-F127, CeO_2-CTAB 和 CeO_2-PEG 样品的比表面积分别为 60.5, 60.2 和 51.8 m^2/g. 具有 3DOM 结构的 CeO_2 样品的低温还原性显著好于无孔的体相 CeO_2，它们的低温还原性按照 CeO_2-PEG < CeO_2-CTAB < CeO_2-F127 的顺序提高，与其表面氧空位密度大小的顺序相吻合. CeO_2 因具有蠕虫状介孔孔壁的 3DOM 结构，改善了其物化性质，使此类材料在催化方面有着更广泛的应用前景.

关键词：双模板法；三维有序大孔；二氧化铈；低温还原性能；蠕虫状介孔孔壁；表面活性剂

中图分类号：O643　　　**文献标识码**：A

Dual-Templating Preparation and Enhanced Low-Temperature Reducibility of Three-Dimensionally Ordered Macroporous Ceria with Mesoporous Walls

ZHANG Han, ZHANG Lei, DENG Jiguang, LIU Yuxi, JIANG Haiyan,

SHI Fengjuan, JI Kemeng, DAI Hongxing[*]

Department of Chemistry and Chemical Engineering, College of Environmental and Energy Engineering,

Beijing University of Technology, Beijing 100124, China

Abstract: Three-dimensionally ordered macroporous (3DOM) ceria with mesoporous walls and cubic crystal structures were prepared with polymethyl methacrylate (PMMA) as a hard template and triblock copolymer Pluronic F127 ($EO_{106}PO_{70}EO_{106}$), cetyltrimethylammonium bromide (CTAB), or poly(ethylene glycol) (PEG) as a soft template. Citric acid was used as a complexing agent and cerium nitrate was used as a metal precursor. The 3DOM CeO_2 samples were characterized by numerous analytical techniques. The as-fabricated CeO_2 samples had a 3DOM architecture with polycrystalline wormhole-like mesoporous walls. The nature of the soft template had an important effect on the pore structure and the surface area of the final product. The surface areas of the F127-, CTAB-, and PEG-derived 3DOM CeO_2 samples (denoted CeO_2-F127, CeO_2-CTAB, and CeO_2-PEG, respectively) were ca. 60.5, 60.2, and 51.8 m^2/g, respectively. The low-temperature reducibility of the 3DOM-structured CeO_2 samples was much better than that of the bulk counterpart and the low-temperature reducibility of the three 3DOM ceria samples increased according to CeO_2-PEG < CeO_2-CTAB < CeO_2-F127, which coincided with the surface oxygen vacancy density sequence. The improved physicochemical properties associated with the formation of the 3DOM skeleton with wormhole-like mesoporous walls may be useful for applications such as CeO_2 materials in heterogeneous catalysis.

Key words: dual-templating preparation method; three-dimensionally ordered macropore; ceria; low-temperature reducibility; wormhole-like mesoporous wall; surfactant

CeO_2 作为催化材料广泛应用于化学和石油工业[1]. 它具有丰富的晶格氧空位、优异的储释氧性能以及低的 Ce^{3+} 和 Ce^{4+} 之间的氧化还原电位,可作为汽车尾气三效催化剂中的储氧材料[2~4],还可作为催化剂应用于甲烷重整和甲烷部分氧化制氢以及水煤气转化制氢反应[2,4],另外还可用作光学材料、高温陶瓷、氧传感器和燃料电池[5~7]. 多孔 CeO_2 具有发达的孔结构、高的比表面积、窄的孔径分布和优异的还原性能,因而显示出更优的性能.

近年来,三维有序大孔 (3DOM) 材料广泛用于电池材料、传感器、催化剂及载体以及生物材料等领域[8,9]. 胶晶模板法是一种有效制备 3DOM 材料的最常见方法,人们利用该方法已制备出具有 3DOM 结构的金属 (Ni, Co, Fe 和 $Ni_{1-x}Co_x$)[10]、金属氧化物 (MgO, Cr_2O_3, Mn_2O_3, Fe_2O_3, Co_3O_4, NiO, ZnO 和 $CaCO_3$)[11]、复合金属氧化物 ($CsAlTiO_4$, $MgAl_2O_4$, $MgFe_2O_4$ 和 $In_{2-x}Mg_xO_3$)[9,12]和钙钛矿型氧化物 ($LaFeO_3$ 和 $La_{1-x}Sr_xFeO_3$)[13,14]. 3DOM CeO_2 具有规整的孔结构和较高的比表面积,表现出独特的物化性质. 因此,建立该材料的可控制备方法具有必要性和重要性. Wu 等[15]以聚苯乙烯 (PS) 微球为硬模板,硝酸铈为金属源,制备出了 3DOM CeO_2; Waterhouse 等[16]以聚甲基丙烯酸甲酯 (PMMA) 微球为硬模板,硝酸铈为金属源,合成了比表面积为 51 m^2/g 的 3DOM CeO_2; 以 PS 为硬模板,硝酸铈或硝酸铈/硝酸铜为金属前驱体,也制得比表面积分别为 38~41 m^2/g 的 3DOM CeO_2[17]和 24 m^2/g 的 3DOM $CuO-CeO_2$[18]. 很显然这些 CeO_2 材料的比表面积均较低.

最近,本课题组利用表面活性剂或柠檬酸辅助的聚甲基丙烯酸甲酯 (PMMA) 模板法合成了 3DOM MgO, 3DOM $\gamma-Al_2O_3$, 3DOM $Ce_{1-x}Zr_xO_2$[19]和 3DOM SiO_2[20],并对其物化性质进行了详细表征. 结果表明,在制备过程中引入表面活性剂或柠檬酸有利于介孔孔壁的形成并可改善其物化性能[19,20]. 本文以 PMMA 为硬模板,三嵌段共聚物 Pluronic F127、十六烷基三甲基溴化铵 (CTAB) 或聚乙二醇 (PEG) 为软模板 (表面活性剂),柠檬酸为络合剂,硝酸铈为金属前驱体,采用双模板法制备 3DOM CeO_2.

1 实验部分

1.1 样品的制备

参照文献 [19],先合成平均孔径为 298 nm 的单分散 PMMA 胶晶微球,再利用软模板 (表面活性剂) 辅助的 PMMA 硬模板法制备具有蠕虫状介孔孔壁 3DOM CeO_2. 将 1.0 g Pluronic F127, 2.1 g 柠檬酸和 4.34 g 硝酸铈溶于 10 g 乙醇水溶液 (乙醇含量 40%),搅拌至溶解,用该溶液浸渍 PMMA 硬模板,待完全浸湿后,多余溶液用布氏漏斗在真空 (0.07 MPa) 下抽滤. 室温干燥 24 h 后,将试样置于瓷舟中,在空气气氛中以 1 °C/min 的速率从室温升至 300 °C 保持 3 h,再升至 500 °C 并在该温度下焙烧 5 h,得到的样品记为 CeO_2-F127. 以 0.1 g CTAB 或 1.0 g PEG-10000 替换 Pluronic F127,同法制得 CeO_2-CTAB 和 CeO_2-PEG 样品. 为了对比,将一定量的 $Ce(NO_3)_3 \cdot 6H_2O$ 在空气中于 500 °C 焙烧 5 h 制备出无孔体相 CeO_2 (记为 bulk-CeO_2).

本文所用化学试剂均为分析纯,购自北京化学试剂公司.

1.2 样品的表征

采用德国 Bruker/AXS 公司 D8 Advance X 射线衍射 (XRD) 仪 (40 kV, 35 mA) 测定样品的晶相结构,Cu 靶, Ni 滤光片 ($\lambda = 0.15406$ nm). 采用 SDT Q600 instrument (TA) 型分析仪,对焙烧前样品进行热重分析 (TGA) 和差热分析 (DSC),在 100 ml/min 的空气气氛中,以 15 °C/min 的速率从室温升至 900 °C. 采用 Gemini Zeiss Supra 55 型扫描电子显微镜 (SEM) 观察样品的形貌及孔结构. 采用日本 JEOL JEM-2010 型透射电子显微镜 (TEM) 摄取样品照片和选区电子衍射 (SAED) 图案. 利用美国 Micromeritics 公司 ASAP 2020 型比表面仪和 Autopore IV 9510 型压汞仪测定

样品的比表面积和孔径分布. 先将样品在 250 °C 真空脱气 3 h, 再在 –196 °C 下测定样品在不同 N_2 相对压力下的吸附量和脱附量, 获得 N_2 吸附-脱附等温线, 由 BET 方程计算样品的比表面积. 利用 X 射线光电子能谱 (XPS, VG CLAM 4 MCD Analyzer) 技术测定样品表面物种中的 Ce 3d, C 1s 和 O 1s 结合能 (E_b), 以 Mg K_α (hv = 1253.6 eV) X 射线作辐射源. 测定前, 先将样品在 20 ml/min 的 O_2 中于 500 °C 焙烧 1 h, 待冷却至室温后, 再用 He 吹扫样品. 处理后的样品先在初级真空室 (1.33×10^{-3} Pa) 脱气 0.5 h, 然后转移到超高真空室 (4×10^{-7} Pa) 进行 XPS 测定. 采用表面污染碳的 C 1s 结合能 (284.6 eV) 来校对样品表面物种中各元素的结合能. 利用美国 Micromeritics 公司 Autochem II 2920 型化学吸附仪对样品进行氢气程序升温还原 (H_2-TPR) 分析, 以测定其还原性. 首先, 将 30 mg CeO_2 样品在 30 ml/min 的空气流中于 450 °C 预处理 1 h. 待冷却至室温后, 样品在 50 ml/min 的 5% H_2-95% Ar (v/v) 混合气流中以 10 °C/min 的速率从室温升至 900 °C, TCD 检测耗氢量. 采用高纯 CuO (Aldrich, 99.995%) 为标样进行定量分析.

2　结果与讨论

2.1　晶体结构

图 1 是各 CeO_2 样品的广角 XRD 谱. 通过与标准 CeO_2 样品的 XRD 谱 (JCPDS 34-0394) 比较后可知, 所有 CeO_2 样品的衍射峰位置与标准谱图相对应. 可见所制备的 CeO_2 样品具有面心立方晶体结构, 各样
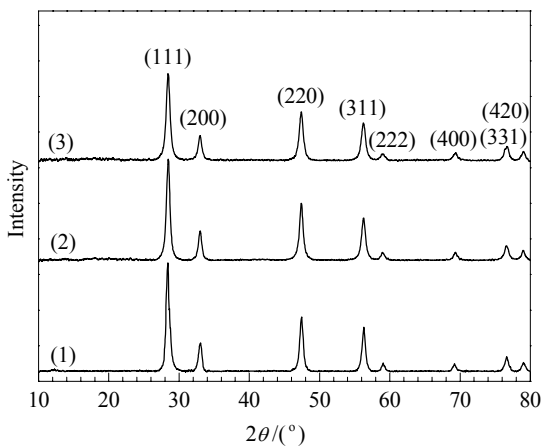

图 1　CeO_2-F127, CeO_2-CTAB 和 CeO_2-PEG 样品的 XRD 谱
Fig. 1. XRD patterns of CeO_2-F127 (1), CeO_2-CTAB (2), and CeO_2-PEG (3).

品衍射峰强度差别不大, 说明其结晶度相似.

图 2 为各 CeO_2 样品在焙烧前的 TGA/DSC 曲线. 由图可见, CeO_2-F127 样品在 210 °C 以下失重 6.6%, 归因于吸附水的脱除[21], 对应的吸热峰位于 136 °C; 在 210~335 和 335~390 °C 之间的失重显著, 分别为 62.8% 和 24.7%, 可归因于硝酸铈的分解、模板 F127 和 PMMA 的氧化分解[10,11,22], 对应的吸热峰分别在 332 和 354 °C. 由于 PMMA 微球在约 290 °C 分解为单体, 在 363 °C 附近发生氧化分解, 所以在 400 °C 以下 PMMA 模板就可被完全去除. CeO_2-CTAB 样品于
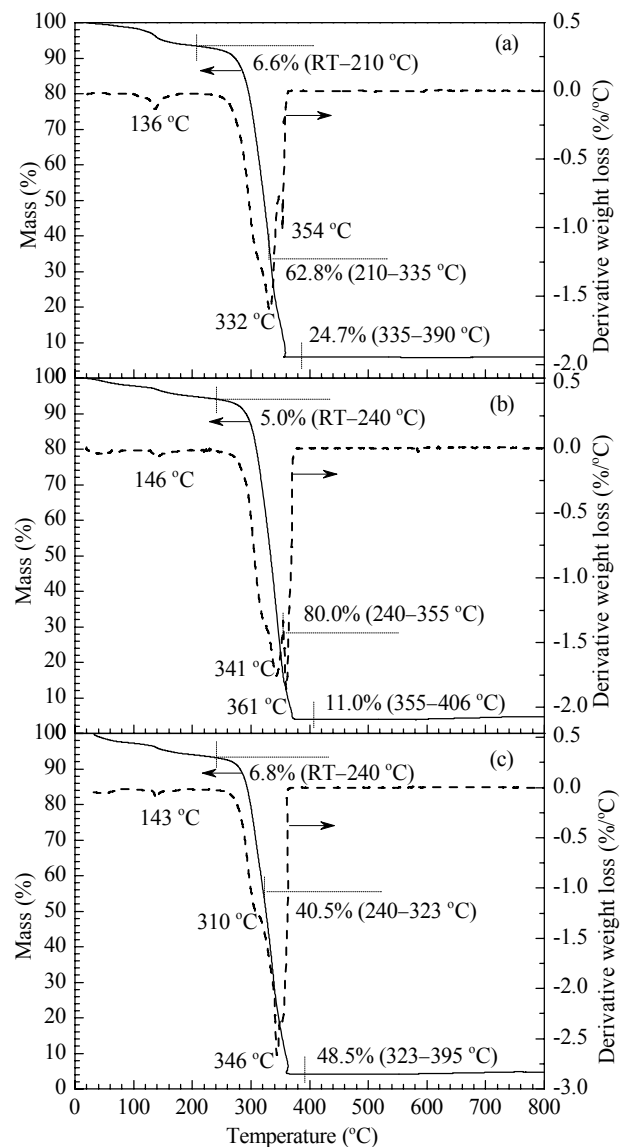

图 2　CeO_2-F127, CeO_2-CTAB 和 CeO_2-PEG 样品在高温焙烧前的 TGA/DSC 曲线
Fig. 2. TGA/DSC profiles of the CeO_2-F127 (a), CeO_2-CTAB (b), and CeO_2-PEG (c) samples before calcination in air.

240 °C 以下失重 5.0%, 归因于吸附水的脱除, 对应的吸热峰位于 146 °C; 另外在 240~355 和 355~406 °C 分别失重 80.0% 和 11.0%, 归因于硝酸铈的分解、模板 CTAB 和 PMMA 的氧化分解, 相应的吸热峰分别在 341 和 361 °C. 而 CeO₂-PEG 样品在 240 °C 以下失重 6.8% 为吸附水的脱除 (吸热峰位于 143 °C); 在 240~323 和 323~395 °C 范围内失重分别为 40.5% 和 48.5%, 为硝酸铈的分解、模板 PEG 和 PMMA 的氧化

分解 (相应的吸热峰位于 310 和 346 °C). 由此可见, 采用 500 °C 焙烧 CeO₂ 前驱物可去除软、硬模板, 得到单相立方结构的 CeO₂ 样品.

2.2　样品形貌、孔结构和比表面积

　　图 3 是各 CeO₂ 样品的 SEM, TEM 照片以及 SAED 图. 可以看出, 所有样品都具有较好的 3DOM 结构, 大孔孔径为 50~200 nm, 孔壁厚度在 15~40 nm 之间. 其孔壁由纳米粒子 (粒径为 4~10 nm) 堆积而

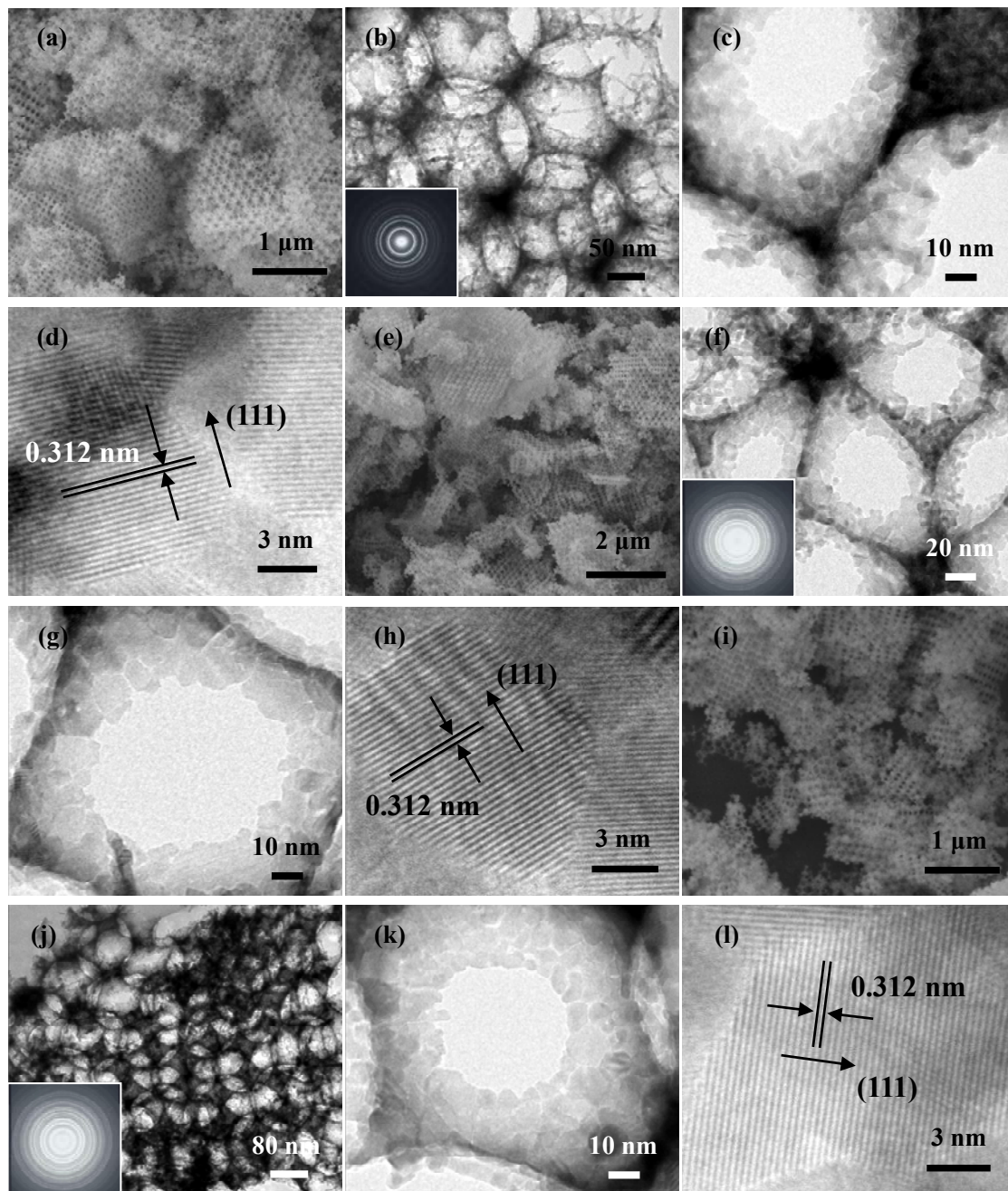
图 3　CeO₂-F127, CeO₂-CTAB 和 CeO₂-PEG 样品的 SEM 照片 (a, e, i), TEM 照片 (b~d, f~h, j~l) 和 SAED 图 (插图)
Fig. 3.　SEM (a, e, i) and TEM (b–d, f–h, j–l) images as well as SAED patterns (insets) of CeO₂-F127 (a–d), CeO₂-CTAB (e–h), and CeO₂-PEG (i–l).

成, 纳米粒子之间形成许多不规则 (类似蠕虫状) 的介孔 (直径为 2~5 nm). 由高分辨 TEM 照片 (见图 3(d), (h) 和 (l)) 可以看出, 各 CeO_2 样品都出现规则的晶格条纹, (111) 晶面间距 d 约为 0.312 nm, 与标准立方相 CeO_2 (JCPDS 34-0394) 的 0.31234 nm 极为相近. 此外, 样品的 SAED 图 (见图 3(b), (f) 和 (j)) 中出现若干明亮而清晰的电子衍射环, 表明其呈多晶态.

图 4(a) 为各 CeO_2 样品的 N_2 吸附-脱附等温线. 可以看出, 制得的 CeO_2 样品具有 II 型吸附等温线, 在相对压力 (p/p_0) 为 0.8~1.0 的范围内形成 H3 滞后环, 在 p/p_0 为 0.2~0.8 的范围内形成一个小的 H2 滞后环. 在 p/p_0 接近 1 附近没有吸附平台的 H3 型滞后环通常意味着该材料中具有狭缝状孔道, 孔径分布延伸至大孔范畴[23]. 在低相对压力区间, 吸附等温线几乎平直的部分由不受限制的单层或多层吸附形成, 意味着该样品具有大孔结构[11]. 另外在 p/p_0 为 0.2~0.8 的范围内样品存在小 H2 型滞后环, 这是由发生在介孔的毛细管凝聚形成的, 表明该样品的大孔孔壁上存在介孔[11,23-25], 这与 TEM 结果一致. 图 4(b) 为采用压汞法测得的 3DOM CeO_2 样品的孔径分布图. 可以看出, 每个 3DOM CeO_2 样品在 50~200 nm 范围内都存在一个较宽的孔径分布, 在峰值为 4~5 nm 处也有一个很窄的孔径分布.

表 1 列出了三个 CeO_2 样品的比表面积以及平均孔径. 由表可见, CeO_2-F127 和 CeO_2-CTAB 样品的比表面积较大, 为 60 m^2/g 左右; 而 CeO_2-PEG 为 51.8 m^2/g. 这与其介孔孔壁的结构有关, 而这正是由于各样品制备所采用表面活性剂的种类不同所致.
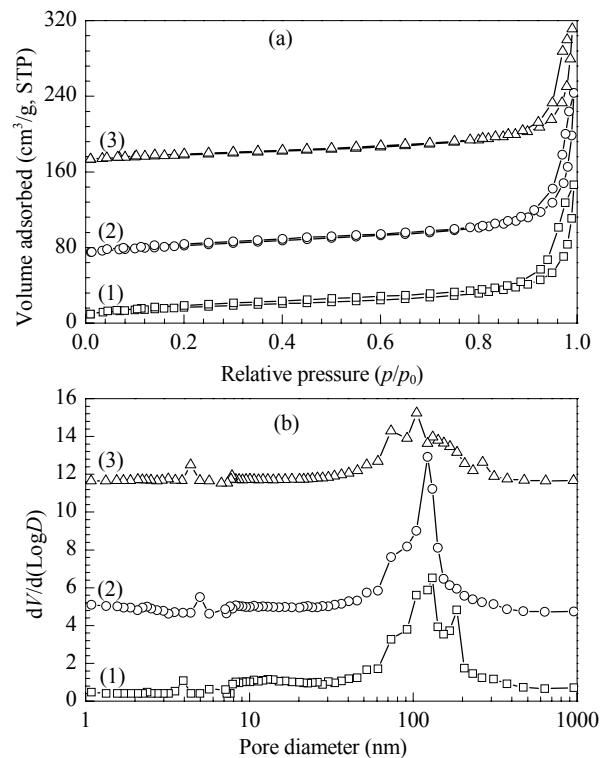

图 4 CeO_2-F127, CeO_2-CTAB 和 CeO_2-PEG 样品的 N_2 吸附-脱附等温线和孔径分布曲线

Fig. 4. N_2 adsorption-desorption isotherms (a) and pore-size distributions (b) of different CeO_2 samples. (1) CeO_2-F127; (2) CeO_2-CTAB; (3) CeO_2-PEG.

CeO_2-F127, CeO_2-CTAB 和 CeO_2-PEG 样品的介孔平均孔径分别为 3.9, 4.9 和 4.3 nm, 而大孔平均孔径则分别为 130, 125 和 120 nm. 蠕虫状介孔结构是由孔壁上 CeO_2 纳米粒子堆积而成, 该介孔结构的存在提高了 3DOM CeO_2 样品的比表面积.

表 1　**3DOM CeO_2 样品的比表面积和平均孔径**

Table 1　BET surface areas and average pore diameters of the three-dimensionally ordered macroporous (3DOM) CeO_2 samples

Sample	A_{BET}[a] (m^2/g)			Average pore diameter[b] (nm)	
	Macropore (> 50 nm)	Mesopore (≤ 50 nm)	Total	Macropore	Mesopore
CeO_2-F127	12.9	47.6	60.5	130	3.9
CeO_2-CTAB	15.6	44.6	60.2	125	4.9
CeO_2-PEG	14.7	37.1	51.8	120	4.3

[a]Data were obtained by using the BET method; [b]Data were obtained by means of the mercury intrusion porosimetry.

2.3　氧物种、铈氧化态和氧空位密度

图 5 为各 3DOM CeO_2 样品的 O 1s 和 Ce 3d XPS 谱. 由图可见, 每个样品的 O 1s 谱在 529.4 和 531.7 eV 处有两个不对称峰, 分别代表表面晶格氧 (O_{latt}) 物种和吸附氧 (O_{ads}, 如 O^-, O_2^{2-} 或 O_2^-) 物种[26]. 通常吸附氧物种位于 CeO_2 的氧空位, 吸附氧物种量越多, 意味着 CeO_2 的氧空位密度更高. 各样品表面 O_{ads}/O_{latt} 摩尔比大小顺序为: CeO_2-F127 > CeO_2-CTAB >> CeO_2-PEG (见表 2). 换句话说, CeO_2-F127 样品和 CeO_2-CTAB 样品比 CeO_2-PEG 样

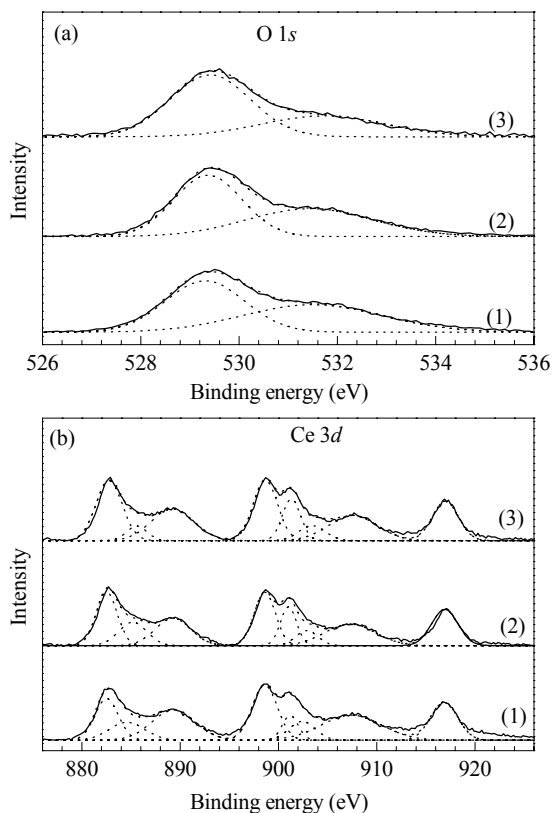**图 5　CeO₂-F127, CeO₂-CTAB 和 CeO₂-PEG 样品的 O 1s 和 Ce 3d XPS 谱**

Fig. 5. O 1s (a) and Ce 3d (b) XPS spectra of different CeO₂ samples. (1) CeO₂-F127; (2) CeO₂-CTAB; (3) CeO₂-PEG.

品具有更高的氧空位密度. 由各样品 Ce 3d XPS 谱可知, 各样品均出现 Ce $3d_{5/2}$ (E_b = 882.8, 885.6, 889.2 和 898.7 eV) 和 Ce $3d_{3/2}$ (E_b = 901.3, 903.1, 907.6 和 917.0 eV) 两组信号. 在 E_b = 885.6 和 903.1 eV 处出现的两个峰可归属为 Ce^{3+}, 而其余峰则可归属为 Ce^{4+}[26~29]. 如表 2 所示, 各样品表面 Ce^{3+}/Ce^{4+} 摩尔比大小顺序为 CeO₂-PEG << CeO₂-CTAB < CeO₂-F127. CeO₂-F127 和 CeO₂-CTAB 样品表面氧空位量比

表 2　3DOM CeO₂ 样品的表面氧和铈组成

Table 2 Surface oxygen and cerium compositions of the 3DOM CeO₂ samples

Sample code	O_{ads}/O_{latt} [a]	Ce^{3+}/Ce^{4+} [b]
CeO₂-F127	0.94	0.17
CeO₂-CTAB	0.84	0.16
CeO₂-PEG	0.52	0.09

[a] O_{ads}/O_{latt} denotes the molar ratio of the surface adsorbed oxygen (O_{ads}) and lattice oxygen (O_{latt}) species of the sample.

[b] Ce^{3+}/Ce^{4+} denotes the molar ratio of surface Ce^{3+} and Ce^{4+} species of the sample.

CeO₂-PEG 样品多, 这与 O 1s 的 XPS 结果相符. 各样品氧空位密度差异是由于其表面 Ce 物种氧化态 (Ce^{3+}/Ce^{4+}) 分布不同所致, 这与制备时所用表面活性剂 (软模板) 种类有关. 氧空位的存在有利于改善 CeO₂ 的还原性能[26,27]. 因此, CeO₂-F127 和 CeO₂-CTAB 样品比 CeO₂-PEG 样品应表现出更好的还原性能.

2.4　还原性能

图 6 为体相 CeO₂ 和各 3DOM CeO₂ 样品的 H₂-TPR 谱. 由图可见, 每个 3DOM CeO₂ 样品的还原过程均可分为两步, 分别位于 250~550 (低温区) 和 550~850 °C (高温区). 体相 CeO₂ 样品在低温区的还原峰弱而宽, 峰值位于 420 °C; 高温区的还原峰峰值位于 800 °C. 三个 3DOM CeO₂ 样品的 H₂-TPR 曲线很相似. (1) 在低温区出现一个较尖锐的还原峰 (峰值为 470 °C), 在 360 °C 检测到一个肩峰, 说明样品中较易还原的 Ce 物种至少存在两种不同的配位环境. CeO₂-F127, CeO₂-CTAB 和 CeO₂-PEG 样品的耗 H₂ 量分别为 740, 725 和 700 μmol/g. (2) 高温区出现一个较宽的还原峰 (峰值为 780 °C), 三个样品对应的耗 H₂ 量分别为 610, 477 和 392 μmol/g. 低温区还原峰可归属为样品表面的 $Ce^{4+}→Ce^{3+}$ 以及表面吸附氧的还原[26,30~32], 高温区还原峰归属于样品体相中的 $Ce^{4+}→Ce^{3+}$ 的还原[26,32]. 基于各样品耗 H₂ 量可以认为, CeO₂ 的低温还原性能顺序为 bulk-CeO₂ <<
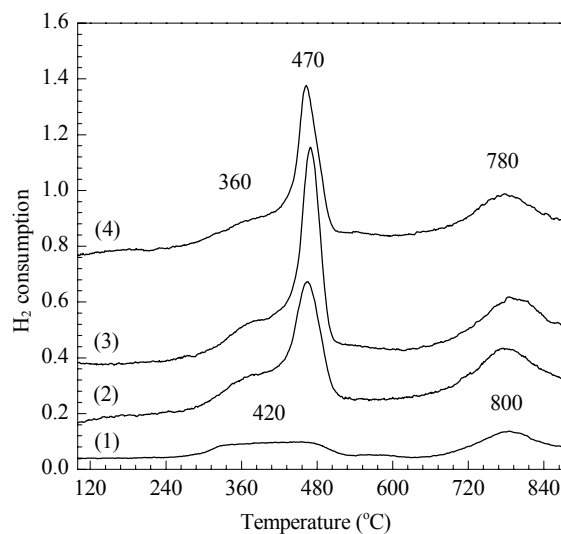
图 6　不同 CeO₂ 样品的 H₂-TPR 谱

Fig. 6. H₂-TPR profiles of different CeO₂ samples. (1) Bulk-CeO₂; (2) CeO₂-F127; (3) CeO₂-CTAB; (4) CeO₂-PEG.

CeO_2-PEG < CeO_2-CTAB < CeO_2-F127. 由此可见，CeO_2 的孔结构和形貌对其低温还原性能影响很大. 换言之，3DOM 结构和蠕虫状介孔孔壁的存在有利于改善 CeO_2 材料的低温还原性.

3 结论

以柠檬酸为络合剂，硝酸铈为金属前驱体，PMMA 为硬模板，F127, CTAB 或 PEG 为软模板，采用双模板法制备了具有蠕虫状介孔孔壁的 3DOM CeO_2. 软模板种类对所制 CeO_2 材料的形貌和孔结构影响很大，在制备过程中引入一定量的表面活性剂可明显增加所制得 CeO_2 样品的比表面积. 3DOM CeO_2 的低温还原性能远远好于体相 CeO, 低温还原性由低到高的顺序为 CeO_2-PEG < CeO_2-CTAB < CeO_2-F127, 这与三个 3DOMCeO_2 样品的表面氧空位密度高低顺序相吻合. 具有蠕虫状介孔孔壁的 3DOM 结构以及独特的物化性质将使 CeO_2 材料在多相催化领域有着更广泛的应用.

参 考 文 献

1 Pedrosa A M G, da Silva J E C, Pimentel P M, Melo D M A, E Silva F R G. *J Alloys Compd*, 2004, **374**: 223

2 Rane N, Zou H, Buelna G, Lin J Y S. *J Membr Sci*, 2005, **256**: 89

3 Gu F B, Wang Zh H, Han D M, Shi Ch, Guo G Sh. *Mater Sci Eng B*, 2007, **139**: 62

4 Sinha A K, Suzuki K. *J Phys Chem B*, 2005, **109**: 1708

5 Zhang G J, Shen Zh R, Liu M, Guo Ch H, Sun P Ch, Yuan Zh Y, Li B H, Ding D T, Chen T H. *J Phys Chem B*, 2006, **110**: 25782

6 Ho Ch M, Yu J C, Kwong T, Mak A C, Lai S. *Chem Mater*, 2005, **17**: 4514

7 Vantomme A, Yuan Zh Y, Du G H, Su B L. *Langmuir*, 2005, **21**: 1132

8 Schroden R C, Blanford C F, Melde B J, Johnson B J S, Stein A. *Chem Mater*, 2001, **13**: 1074

9 Madhavi S, Ferraris C, White T. *J Solid State Chem*, 2006, **179**: 866

10 Yan H W, Blanford C F, Lytle J C, Carter C B, Smyrl W H, Stein A. *Chem Mater*, 2001, **13**: 4314

11 Yan H W, Blanford C F, Holland B T, Smyrl W H, Stein A. *Chem Mater*, 2000, **12**: 1134

12 Zou L, Xiang X, Fan J, Li F. *Chem Mater*, 2007, **19**: 6518

13 Sadakane M, Horiuchi T, Kato N, Sasaki K, Ueda W. *J Solid State Chem*, 2010, **183**: 1365

14 Sadakane M, Asanuma T, Kubo J, Ueda W. *Chem Mater*, 2005, **17**: 3546

15 Wu Q Z, Shen Y, Liao J F, Li Y G. *Mater Lett*, 2004, **58**: 2688

16 Waterhouse G I N, Metson J B, Idriss H, Sun-Waterhouse D X. *Chem Mater*, 2008, **20**: 1183

17 Zhang J, Jin Y, Li Ch Y, Shen Y N, Han L, Hu Zh X, Di X W, Liu Zh L. *Appl Catal B*, 2009, **91**: 11

18 Zhang Y, Liang H, Gao X Y, Liu Y. *Catal Commun*, 2009, **10**: 1432

19 Li H N, Zhang L, Dai H X, He H. *Inorg Chem*, 2009, **48**: 4421

20 Li H N, Dai H X, He H. *J Sci Conf Proc*, 2009, **1**: 186

21 邬泉周, 尹强, 廖菊芳, 邓景衡, 李玉光. 化学学报 (Wu Q Zh, Yin Q, Liao J F, Deng J H, Li Y G. *Acta Chim Sin*), 2005, **63**: 891

22 Yan H W, Zhang K, Blanford C F, Francis L F, Stein A. *Chem Mater*, 2001, **13**: 1374

23 Li W C, Lu A H, Weidenthaler C, Schüth F. *Chem Mater*, 2004, **16**: 5676

24 Matos J R, Kruk M, Mercuri L P, Jaroniec M, Zhao L, Kamiyama T, Terasaki O, Pinnavaia T J, Liu Y. *J Am Chem Soc*, 2003, **125**: 821

25 Gulková D, Šolcová O, Zdražil M. *Microporous Mesoporous Mater*, 2004, **76**: 137

26 Zhang Y J, Zhang L, Deng J G, Dai H X, He H. *Inorg Chem*, 2009, **48**: 2181

27 Mašek K, Václavů M, Bábor P, Matolín V. *Appl Surf Sci*, 2009, **255**: 6656

28 Wang R P, Pan Sh H, Zhou Y L, Zhou G W, Liu N N, Xie K, Lu H B. *J Cryst Growth*, 1999, **200**: 505

29 Escamilla-Perea L, Nava R, Pawelec B, Rosmaninho M G, Peza-Ledesma C L, Fierro J L G. *Appl Catal A*, 2010, **381**: 42

30 Zhou K B, Wang X, Sun X M, Peng Q, Li Y D. *J Catal*, 2005, **229**: 206

31 Pérez-Hernández R, Gutiérrez-Martínez A, Gutiérrez-Wing C E. *Int J Hydrogen Energy*, 2007, **32**: 2888

32 Caputo T, Lisi L, Pirone R, Russo G. *Appl Catal A*, 2008, **348**: 42

英 译 文
English Text

Ceria is a catalytic material that is used in the chemical and petrochemical industries [1]. Because of the good oxygen storage capacity (OSC) associated with the rich oxygen vacancies and the low redox potential between Ce^{3+} and Ce^{4+}, CeO_2 has been used as a promoter in three-way catalysts for the removal of automotive exhaust gases [2–4] and as a catalyst for the reforming and partial oxidation of methane and the water-gas shift during "on board" hydrogen produc-

tion [2,4]. Ceria is also applied as an optical material in high-temperature ceramics, as oxygen sensors, and as fuel cells [5–7]. Porous ceria with good porosity, a high surface area, a narrow pore-size distribution, and good reducibility is expected to possess improved properties.

Three-dimensionally ordered macroporous (3DOM) materials have attracted a large amount of attention lately because of their potential use as battery materials, sensors, catalysts or supports, and biomaterials [8,9]. To date, the colloidal crystal templating method is a commonly adopted pathway to obtain 3DOM materials with metals (Ni, Co, Fe, and $Ni_{1-x}Co_x$) [10], metal oxides (MgO, Cr_2O_3, Mn_2O_3, Fe_2O_3, Co_3O_4, NiO, ZnO, and $CaCO_3$) [11], mixed metal oxides ($CsAlTiO_4$, $MgAl_2O_4$, $MgFe_2O_4$, and $In_{2-x}Mg_xO_3$) [9,12], and perovskite-type oxides ($LaFeO_3$ and $La_{1-x}Sr_xFeO_3$) [13,14]. 3DOM-structured CeO_2 possesses an ordered pore architecture and a high surface area, which gives these materials unique physicochemical properties. Therefore, it is highly desirable to establish an effective strategy for the controlled preparation of 3DOM CeO_2. Several reports exist about the fabrication of 3DOM CeO_2. For example, Wu et al. [15] prepared 3DOM CeO_2 using well-aligned polystyrene (PS) microspheres as a hard template and cerium nitrate as a metal precursor. Waterhouse et al. [16] used polymethyl methacrylate (PMMA) as a hard template and cerium nitrate as a cerium source to generate a 3DOM CeO_2 material with a surface area of 51 m^2/g. With PS as a hard template and cerium and/or copper nitrates as a metal precursor, Zhang et al. obtained 3DOM CeO_2 with a surface area of ca. 38–41 m^2/g [17] and 3DOM CuO-CeO_2 with a surface area of 24 m^2/g [18]. Obviously, the surface areas of these 3DOM materials are relatively low.

Previously, our group investigated the synthesis, characterization, and physicochemical properties of various 3DOM-structured materials with high surface areas such as MgO (surface area = 243 m^2/g), γ-Al_2O_3 (surface area = 145 m^2/g), $Ce_{1-x}Zr_xO_2$ (surface area = 100 m^2/g) [19], and SiO_2 (surface area = 663 m^2/g) [20] using the surfactant- and/or the citric acid-assisted PMMA-templating method. We found that the introduction of a surfactant or citric acid during the synthesis process is beneficial for the formation of mesoporous walls and thus for the synthesis of 3DOM-structured materials with the desired physicochemical properties [19,20]. Recently, we extended our attention to the fabrication of 3DOM-structured rare earth oxides with high surface areas. In this work, we report a facile dual-templating preparation method to obtain a 3DOM-structured CeO_2 material with wormhole-like mesoporous walls and excellent low-temperature reducibility by employing PMMA as a hard template and the triblock copolymer Pluronic F127 ($EO_{106}PO_{70}EO_{106}$), cetyltrimethylammonium bromide (CTAB), or poly(ethylene glycol) (PEG) as a soft template.

Citric acid was used as the complexing agent and cerium nitrate was used as the metal precursor. We found that the 3DOM CeO_2 derived with F127 had the highest surface area of ca. 61 m^2/g and the best low-temperature reducibility.

1 Experimental

1.1 Fabrication of 3DOM-structured CeO_2 with wormhole-like mesoporous walls

Uniform monodispersed PMMA colloid crystal microspheres with an average pore diameter of 298 nm were synthesized using the method described previously [19]. 3DOM-structured CeO_2 with mesoporous walls were prepared using the surfactant-assisted PMMA-templating strategy. Typical fabrication procedures were as follows. 1.0 g of Pluronic F127 or PEG-10000 or 0.1 of CTAB, 2.1 g of citric acid, and 4.34 g of $Ce(NO_3)_3 \cdot 6H_2O$ were dissolved in 10.0 g of ethanol aqueous solution (40 wt%) while stirring. After dissolution, 2.0 g of highly ordered PMMA colloidal crystal microspheres was added and suspended in the above mixed solution. After the PMMA microspheres were thoroughly wetted, the excessive liquid was filtered using a Buchner funnel connected to a vacuum (0.07 MPa). After drying at room temperature (RT) for 24 h, the 3DOM materials were obtained by calcination in air at a heating rate of 1 °C/min from RT to 300 and 500 °C and maintained at these two temperatures for 3 and 5 h, respectively. The obtained samples were denoted CeO_2-F127, CeO_2-PEG, and CeO_2-CTAB, respectively. The bulk ceria (denoted bulk-CeO_2) sample was also prepared by calcining a certain amount of $Ce(NO_3)_3 \cdot 6H_2O$ in air at 500 °C for 5 h for comparison.

All the chemicals used in this work were from Beijing Chemical Reagent Company and were of analytical grade and used without further purification.

1.2 Sample characterization

The crystal structures of the samples were determined using a Bruker/AXS D8 Advance X-ray diffractometer (XRD) operated at 40 kV and 35 mA with Cu K_α radiation and a nickel filter (λ = 0.15406 nm). The crystal phases were identified by referring to standard XRD data from the JCPDS database. Thermogravimetric analysis (TGA) and differential scanning calorimetric (DSC) analysis of the uncalcined samples were carried out on a SDT Q600 (TA) apparatus in an air flow of 100 ml/min from RT to 900 °C using a ramp of 10 °C/min. The scanning electron microscope (SEM) images were recorded on a Gemini Zeiss Supra 55 operated at 10 kV. Transmission electron microscopy (TEM) images as well as selected-area electron diffraction (SAED) patterns of the

samples were obtained using a JEOL JEM-2010. The surface areas of the samples were measured by N_2 adsorption at −196 °C on a Micromeritics ASAP 2020 adsorption analyzer. Before measurement, the samples were outgassed at 250 °C for 3 h. The surface areas were calculated using the Brunauer-Emmett-Teller (BET) method. The pore-size distributions of the 3DOM CeO_2 samples were determined by mercury intrusion porosimetry (Autopore IV 9510). X-ray photoelectron spectroscopy (XPS, VG CLAM 4 MCD Analyzer) was used to determine the Ce $3d$, O $1s$, and C $1s$ binding energies (E_b) of the surface species with Mg K_α (hv = 1253.6 eV) as the excitation source. Before XPS analysis, the samples were calcined in O_2 (flow rate = 20 ml/min) at 500 °C for 1 h and then cooled to RT. After this pretreatment, the samples were mounted and transferred to a spectrometer in a transparent glove bag (Instruments for Research and Industry, USA) that was filled with helium. The samples were then outgassed in the preparation chamber (1.33 × 10^{-3} Pa) for 0.5 h and placed in the analysis chamber (4 × 10^{-7} Pa) for spectrum recording. The C $1s$ signal at 284.6 eV was taken as a reference for E_b calibration. Hydrogen temperature-programmed reduction (H_2-TPR) experiments were conducted on a chemical adsorption analyzer (Autochem II 2920, Micromeritics). Before the TPR measurement, 30 mg of the CeO_2 sample was first treated in an air flow of 30 ml/min at 450 °C for 1 h in a quartz fixed-bed U-shaped microreactor (i.d. = 4 mm). After cooling to RT in the same atmosphere, the pretreated sample was exposed to a 50 ml/min flow of a 5% H_2-95% Ar (v/v) mixture and heated to 900 °C at a ramp of 10 °C/min. The change in H_2 concentration of the effluent was monitored on-line by a chemical adsorption analyzer. The reduction band was calibrated by the complete reduction of standard powdered CuO (Aldrich, 99.995%).

2 Results and discussion

2.1 Crystal structure

Figure 1 shows the XRD patterns of the 3DOM CeO_2 samples prepared under different conditions. By comparison to a XRD pattern of a standard CeO_2 sample (JCPDS 34-0394) the XRD lines of all of the 3DOM CeO_2 samples were well indexed, as indicated in Fig. 1(3). Therefore, it is reasonable to deduce that the as-fabricated CeO_2 samples possess a cubic crystal structure. Small differences in diffraction intensity were apparent for the three 3DOM CeO_2 samples indicating that they possessed similar crystallinity.

Figure 2 shows the TGA/DSC profiles of the 3DOM CeO_2 samples before calcination in air at high temperature. For the uncalcined CeO_2-F127 sample (Fig. 2(a)), a small weight loss (ca. 6.6 wt%) was apparent below 210 °C, and this was assignable to the removal of adsorbed water [21]. This was

accompanied by the appearance of an endothermic peak at 136 °C and two significant weight losses (ca. 62.8 wt% in the 210–335 °C range and ca. 24.7 wt% in the 335–390 °C range) because of the thermal decomposition of $Ce(NO_3)_3$ and the elimination of the F127 and PMMA templates [10,11,22]. This was in addition to the endothermic peaks at 332 and 354 °C, respectively. Since PMMA microspheres dissociate at ca. 290 °C and become oxygenolyzed at around 363 °C it is reasonable to assume that the PMMA template could be totally removed below 400 °C. For the uncalcined CeO_2-CTAB sample (Fig. 2(b)), a weight loss of ca. 5.0 wt% below 240 °C because of the removal of adsorbed water in addition to an endothermic peak at 146 °C was evident. The other two weight losses of ca. 80.0 wt% in the 240–355 °C range and ca. 11.0 wt% in the 355–406 °C range is attributed to the thermal decomposition of $Ce(NO_3)_3$ and the elimination of the CTAB and PMMA templates, which corresponds to the endothermic peaks at 341 and 361 °C, respectively. As for the uncalcined CeO_2-PEG sample (Fig. 2(c)), a weight loss of ca. 6.8 wt% below 240 °C because of adsorbed water removal (with the appearance of a weak endothermic signal at 143 °C) and two weight losses of ca. 40.5 wt% in the 240–323 °C range and ca. 48.5 wt% in the 323–395 °C range is attributed to the thermal decomposition of $Ce(NO_3)_3$ and the elimination of the PEG and PMMA templates (corresponding to the endothermic peaks at 310 and 346 °C). These results indicate that the final calcination temperature (500 °C) used in this work was high enough for the removal of the hard and soft templates and for the formation of single-phase cubic 3DOM CeO_2.

2.2 Morphology, pore structure, and surface area

Figure 3 shows representative SEM and TEM images as well as SAED patterns of the as-prepared CeO_2 samples. We observed that all the samples had a high-quality 3DOM structure with macropore sizes of 50–200 nm, and the typical wall thickness was in the range of 15–40 nm. The walls of the 3DOM CeO_2 samples were composed of relatively uniform nanoparticles (diameter = 4–10 nm) among which numerous wormhole-like mesopores (diameter = 2–5 nm) were present. As can be seen from the high-resolution TEM images (Figs. 3(d), (h), and (l)), there were well-resolved lattice fringes with lattice spacings (d value) of the (111) plane being 0.312 nm for each of the 3DOM CeO_2 samples. This is rather close to that (0.31234 nm, JCPDS 34-0394) of the standard cubic CeO_2 sample. Furthermore, the recording of multiple bright electron diffraction rings in the SAED patterns (insets of Figs. 3(b), (f), and (j)) means that all the 3DOM CeO_2 samples were polycrystalline.

Figure 4(a) shows the N_2 adsorption-desorption isotherms of the 3DOM CeO_2 samples. The isotherms of the samples

have a type II isotherm with a big H3 hysteresis loop in the relative pressure (p/p_0) range of 0.8–1.0. They also have a small H2 type hysteresis loop in the p/p_0 range of 0.2–0.8. The H3 hysteresis loop, which did not clearly show any adsorption plateau at p/p_0 close to unity is related to the existence of slit-shaped pores in the materials, which is indicative of a pore-size distribution that extends to the macropore range [23]. The low-pressure portion of the almost linear middle section of the isotherm, which can be attributed to unrestricted mono- or multilayer adsorption suggests that the samples were macroporous [11]. The H2 hysteresis loop in the p/p_0 range of 0.2–0.8, linkable to the capillary condensation taking place in mesopores indicates that mesopores exist in the wall structure [11,23–25]. This was confirmed by the results of TEM investigations (Fig. 3). Figure 4(b) shows the pore-size distributions of the 3DOM CeO_2 samples that were measured by Hg porosimetry. Each of the three samples exhibited a rather narrow pore-size distribution centered at ca. 4–5 nm and a broad pore-size distribution that was scattered from 50 to 200 nm.

The BET surface areas and pore-size distributions of the 3DOM CeO_2 samples that were synthesized under different conditions are summarized in Table 1. We found that the nature of the surfactant had an impact on the textural property of the samples. The 3DOM CeO_2 samples had surface areas of 51.8–60.5 m^2/g with the CeO_2-F127 and CeO_2-CTAB samples having higher surface areas. The discrepancy in surface area might be associated with the difference in the mesoporous wall structures of the 3DOM CeO_2 materials, which were dependent on the nature of the surfactant adopted. For the CeO_2-F127, CeO_2-CTAB, and CeO_2-PEG samples, the average mesopore diameter was ca. 3.9, 4.9, and 4.3 nm, respectively. The corresponding macropore diameter was ca. 130, 125, and 120 nm. The presence of wormhole-like mesopores that formed because of the aggregation of CeO_2 nanoparticles in the walls of the samples was responsible for the increase in surface area (Table 1).

2.3 Oxygen species, cerium oxidation state, and oxygen vacancy density

Figure 5 illustrates the O 1s and Ce 3d XPS spectra of the 3DOM CeO_2 samples. Figure 5(a) shows that the O 1s spectrum of each of the 3DOM CeO_2 samples could be deconvoluted into two components at E_b = 529.4 and 531.7 eV, which is attributable to the surface lattice oxygen (O_{latt}) and the adsorbed oxygen (O_{ads}, e.g. O^-, O_2^{2-}, or O_2^-) species [26], respectively. The O_{ads} species are usually present at the oxygen vacancies of CeO_2. A large amount of O_{ads} species implies a higher oxygen vacancy density. The surface O_{ads}/O_{latt} molar ratio decreased as follows: CeO_2-F127 > CeO_2-CTAB >> CeO_2-PEG (Table 2). In other words, the

CeO_2-F127 and CeO_2-CTAB samples possessed much higher surface oxygen vacancy densities than the CeO_2-PEG sample. Figure 5(b) shows that two sets of signals are present: one set centered at E_b = 882.8, 885.6, 889.2, and 898.7 eV, assignable to Ce 3$d_{5/2}$, and the other centered at E_b = 901.3, 903.1, 907.6, and 917.0 eV, assignable to Ce 3$d_{3/2}$ [26–29]. The signals at E_b = 885.6 and 903.1 eV are due to Ce^{3+} whereas those at the other E_bs are due to Ce^{4+} [26,27,29]. As shown in Table 2, the surface Ce^{3+}/Ce^{4+} molar ratio increases as follows: CeO_2-PEG << CeO_2-CTAB < CeO_2-F127. This order suggests that there are larger amounts of surface oxygen vacancies on the CeO_2-CTAB and CeO_2-F127 samples than on the CeO_2-PEG sample. This is in good agreement with the O 1s XPS results. The discrepancy in surface oxygen vacancy density of these samples is due to the difference in the surface cerium oxidation state distribution, which might be induced by surfactants (soft templates) of different nature. It is well accepted that the presence of oxygen vacancies is favorable for an improvement in the reducibility of ceria [26,27]. Therefore, the CeO_2-CTAB and CeO_2-F127 samples are expected to have much better reducibility than the CeO_2-PEG sample, as substantiated by the TPR results below.

2.4 Reducibility

Figure 6 shows the H_2-TPR profiles of the bulk and 3DOM CeO_2 samples. Two reduction steps are present for each sample: a low-temperature step in the range of 250–550 °C and a high-temperature step in the range of 550–850 °C. The bulk CeO_2 sample showed one rather weak and broad reduction band centered at 420 °C and one weak reduction band centered at 800 °C. Its H_2 consumption was 290 and 177 μmol/g, respectively. The 3DOM CeO_2 samples had similar reduction features. (i) One sharp reduction-band is present at 470 °C with a shoulder at 360 °C, which suggests the existence of at least two kinds of cerium species in the different coordination environments and the H_2 consumption was 740, 725, and 700 μmol/g for the 3DOM-structured CeO_2-F127, CeO_2-CTAB, and CeO_2-PEG samples, respectively. (ii) One broad reduction band is centered at 780 °C and the corresponding H_2 consumption is 610, 477, and 392 μmol/g. The low-temperature reduction band is attributable to the reduction of surface Ce^{4+} to Ce^{3+} as well as the removal of a small amount of oxygen adspecies [26,30–32] whereas the high-temperature reduction band is attributable to the reduction of bulk Ce^{4+} to Ce^{3+} [26,32]. Based on the H_2 consumption of these samples, the low-temperature reducibility increased as follows: bulk-CeO_2 << CeO_2-PEG < CeO_2-CTAB < CeO_2-F127. These results indicate that the pore structure and morphology significantly affect the low-temperature reducibility of CeO_2. In other words, the

presence of the 3DOM architecture with wormhole-like mesoporous walls is beneficial for the low-temperature reducibility of the ceria material.

3 Conclusions

Using the dual-templating strategy with PMMA as a hard template and F127, CTAB, or PEG individually as soft templates, citric acid as a complexing agent and cerium nitrate as a metal source, it is possible to generate 3DOM-structured CeO_2 materials with wormhole-like mesoporous walls. The nature of the soft template greatly influences the morphology and porous structure of the obtained CeO_2 samples. The addition of a certain amount of F127, CTAB, or PEG to the precursor solution during the preparation process can markedly enhance the surface area of the 3DOM ceria sample. The 3DOM-structured ceria samples have much better low-temperature reducibility than their bulk counterparts. Among the three 3DOM ceria samples, the low-temperature reducibility increased as follows: CeO_2-PEG < CeO_2-CTAB < CeO_2-F127. This order is in good agreement with their surface oxygen vacancy density order. The unique physico-chemical properties and behavior related to the presence of 3DOM architecture with wormhole-like mesoporous walls can potentially be used in heterogeneous catalysis.

Acknowledgments